The Astrophysical Journal, 849:140 (12pp), 2017 November 10 https://doi.org/10.3847/1538-4357/aa8ee0

Two-dimensional Molecular Gas and Ongoing Star Formation around H II Region Sh2-104

Jin-Long Xu[1], Ye Xu[2,3], Naiping Yu[1], Chuan-peng Zhang[1], Xiao-Lan Liu[1], Jun-Jie Wang[1], Chang-chun Ning[4], Bing-Gang Ju[3], and Guo-Yin Zhang[1]

[1] National Astronomical Observatories, Chinese Academy of Sciences, Beijing 100012, China; xujl@bao.ac.cn
[2] Purple Mountain Observatory, Chinese Academy of Sciences, Nanjing 210008, China
[3] Purple Mountain Observatory, Qinghai Station, 817000, Delingha, China
[4] Tibet University, Lhasa, Tibet 850000, China

Received 2017 April 7; revised 2017 September 16; accepted 2017 September 21; published 2017 November 8

Abstract

We performed a multi-wavelength study toward H II region Sh2-104. New maps of ^{12}CO $J = 1 - 0$ and ^{13}CO $J = 1 - 0$ were obtained from the Purple Mountain Observatory 13.7 m radio telescope. Sh2-104 displays a double-ring structure. The outer ring with a radius of 4.4 pc is dominated by 12, 500 μm, ^{12}CO $J = 1 - 0$, and ^{13}CO $J = 1 - 0$ emission, while the inner ring with a radius of 2.9 pc is dominated by 22 μm and 21 cm emission. We did not detect CO emission inside the outer ring. The north–east portion of the outer ring is blueshifted, while the south–west portion is redshifted. The present observations have provided evidence that the collected outer ring around Sh2-104 is a two-dimensional structure. From the column density map constructed by the Hi-GAL survey data, we extract 21 clumps. About 90% of all the clumps will form low-mass stars. A power-law fit to the clumps yields $M = 281\ M_{\odot}(r/\mathrm{pc})^{1.31\pm0.08}$. The selected YSOs are associated with the collected material on the edge of Sh2-104. The derived dynamical age of Sh2-104 is 1.6×10^6 yr. Comparing the Sh2-104 dynamical age with the YSO timescale and the fragmentation time of the molecular ring, we further confirm that the collect-and-collapse process operates in this region, indicating positive feedback from a massive star for surrounding gas.

Key words: H II regions – ISM: clouds – stars: early-type – stars: formation

1. Introduction

OB stars emit copious ultraviolet (UV) photons. UV photons with energies above 13.6 eV can ionize hydrogen to create an H II region. Since the gas pressure inside H II regions is higher than that of their surrounding neutral medium, the H II regions expand. Expanding H II regions will also reshape their surrounding molecular gas, and thereby regulate star formation in the molecular gas. Accordingly, it plays two roles. One is the destructive role, where it can can evaporate or disperse the surrounding molecular gas and consequently terminate star formation, and another is the constructive role, where it can trigger star formation.

At present two main processes have been put forward for triggering star formation at the peripheries of H II regions: collect-and-collapse (CC) and radiation-driven implosion (RDI; Elmegreen & Lada 1977; Deharveng et al. 2010). In the CC process, a compressed layer of neutral material is accumulated between the ionization front and shock front, and star formation occurs when this layer becomes gravitationally unstable. Unlike the CC process, in the RDI process a pre-existing denser gas is compressed by the shocks, and then forms stars. The CC process is more attractive because it allows the formation of massive stars or clusters (Deharveng et al. 2005). To investigate the star formation triggered by the CC process, several individual H II regions have been studied, such as Sh 104 (Deharveng et al. 2003), RCW 79 (Zavagno et al. 2006), RCW 120 (Zavagno et al. 2007), Sh2-212 (Deharveng et al. 2008), Sh2-217 (Brand et al. 2011), Sh2-90 (Samal et al. 2014), Sh2-87 (Xu & Ju 2014), N6 (Yuan et al. 2014), and Gum 31 (Duronea et al. 2015). Moreover, there are also some statistical studies of infrared bubbles (e.g., Deharveng et al. 2010; Kendrew et al. 2012; Thompson et al. 2012; Kendrew et al. 2016), which are created by the expanding H II regions. A common feature of the above studies is that several massive fragments are found on the border of each H II region. Some star formation activity has been detected in these fragments, such as outflow, UCH II, and water masers. Generally, if an expanding H II region collects its surrounding gas, the morphology of the molecular gas will show three-dimensional spherical structure. CO observations can provide velocity information to reveal the gas structure surrounding the H II regions. Beaumont & Williams (2010) observed 43 infrared bubbles using the CO molecular line, but they did not detect the front and back faces of these shells at blueshifted and redshifted velocities. Hence, they concluded that the bubbles enclosing H II regions are two-dimensional rings formed in parental molecular clouds with thicknesses not greater than the bubble sizes. However, molecular gas with a three-dimensional spherical structure or a two-dimensional ring around H II region is important for understanding the triggered star formation (Deharveng et al. 2015).

Sh2-104 is an optically visible Galactic H II region with a 7′ diameter. The distance to Sh2-104 is ~4 kpc (Deharveng et al. 2003). This H II region is excited by an O6V center star (Crampton et al. 1978; Lahulla 1985), whose ionized gas has a local standard of rest (LSR) velocity of 0 km s^{-1} (Georgelin et al. 1973). Sh2-104 displays a shell-like morphology, detected at optical and radio wavelengths. Using *Herschel* data, Rodón et al. (2010) found that the dust temperature is ~25 K in the PDR of Sh2-104, while it is ~40 K in its interior. Deharveng et al. (2003) detected a molecular shell with four large molecular condensations around Sh2-104. A UCH II region lies at an eastern condensation, which is associated with IRAS 20160+3636. A high CN/HCN ratio in the eastern condensation suggests that the condensation is affected by

Sh2-104 (Minh et al. 2014). A near-IR cluster lies in the UCH II direction (Deharveng et al. 2003). The massive condensations and cluster around Sh2-104 suggest that this H II region is a typical candidate for triggering star formation by the CC process.

In this paper, we performed a multi-wavelength study to further investigate the gas structure and star formation around H II region Sh2-104. The molecular gas associated with Sh 104 was observed in ^{12}CO $J = 2 - 1$, ^{13}CO $J = 1 - 0$, and C^{18}O $J = 1 - 0$ with the IRAM 30 m telescope (Deharveng et al. 2003). However, they did not provide maps of the ^{13}CO $J = 1 - 0$ and C^{18}O $J = 1 - 0$ molecular gas in their paper. New maps of ^{12}CO $J = 1 - 0$ and ^{13}CO $J = 1 - 0$ were shown from the Purple Mountain Observatory (PMO) 13.7 m radio telescope. Combining our data with those obtained by the NRAO VLA Sky survey, the Hi-GAL survey, and the *Wide-field Infrared Survey Explorer* (*WISE*) survey, our aim was to construct a comprehensive large-scale picture of Sh2-104. Our observations and data reduction are described in Section 2.1, and the results are presented in Section 3. In Section 4, we discuss the gas structure around Sh2-104 and the star formation scenario, and our conclusions are summarized in Section 5.

2. Observation and Data Processing

2.1. Archival Data

We used far-infrared data (70 μm $\sim$ 500 μm) from the *Herschel* Infrared Galactic Plane survey (Hi-GAL; Molinari et al. 2010) carried out by the *Herschel* Space Observatory. The initial survey covered a Galactic longitude region of $300^\circ < \ell < 60^\circ$ and $|b| < 1\overset{\circ}{.}0$. The Hi-GAL survey used two instruments, PACS (Poglitsch et al. 2010) and SPIRE (Griffin et al. 2010), in parallel mode, to carry out a survey of the inner Galaxy in five bands: 70, 160, 250, 350, and 500 μm. The scan speed of PACS is 20″ per second, while the speed is 30″ per second for SPIRE. The angular resolutions of these five bands are 10.″7, 11.″4, 18.″2, 24.″9, and 36.″3, respectively. These Hi-GAL data have been used to explore the flux density distribution and to construct a column density map of the studied region.

The 1.4 GHz radio continuum emission data were obtained from the NRAO VLA Sky Survey (NVSS; Condon et al. 1998), which is a 1.4 GHz continuum survey covering the entire sky north of -40° declination with a noise of about 0.45 mJy/beam and a resolution of 45″.

We also utilized infrared data from the *WISE* survey (Wright et al. 2010). The *WISE* survey maps the whole sky in four infrared bands, 3.4 μm (*W*1), 4.6 μm (*W*2), 12 μm (*W*3), and 22 μm (*W*4), at angular resolutions of 6.″1, 6.″4, 6.″5, and 12″, respectively.

2.2. Purple Mountain Data

We also conducted the mapping observations of H II region Sh2-104 and its adjacent region in the transitions of ^{12}CO $J = 1 - 0$, ^{13}CO $J = 1 - 0$, and C^{18}O $J = 1 - 0$ lines using the Purple Mountain Observation (PMO) 13.7 m radio telescope at De Ling Ha in the west of China at an altitude of 3200 m, during 2016 December. The 3×3 beam array receiver system in single-sideband mode was used as a front end. The back end was a fast Fourier transform spectrometer of 16384 channels with a bandwidth of 1 GHz, corresponding to a velocity resolution of 0.16 km s^{-1} for ^{12}CO $J = 1 - 0$, and 0.17 km s^{-1} for ^{13}CO $J = 1 - 0$ and C^{18}O $J = 1 - 0$. ^{12}CO

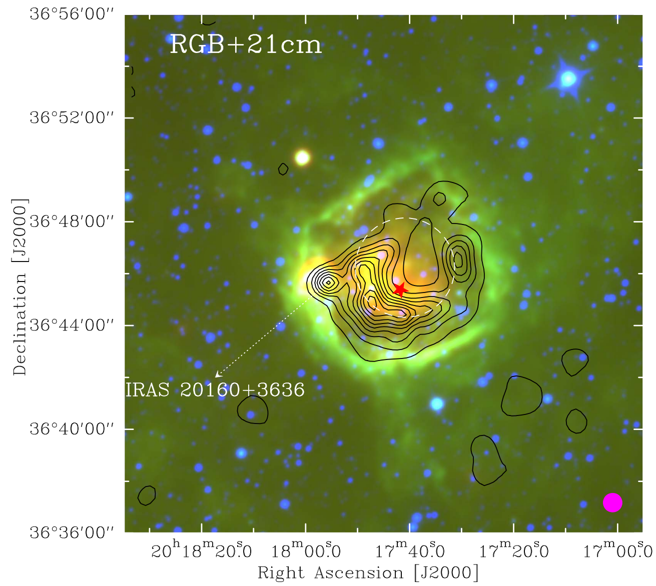

Figure 1. 1.4 GHz radio continuum contours are in black, overlaid on a three-color image of H II Sh2-104 composed from the *WISE* 3.4 μm, 12 μm, and 22 μm bands in blue, green, and red, respectively. The black contours begin at 5σ in steps of 10σ, with $1\sigma = 0.7$ mJy beam^{-1}. The white dashed circle indicates an ionized gas ring for Sh2-104. The red "star" marks the position of the exciting star.

$J = 1 - 0$ was observed at an upper sideband with a system noise temperature (Tsys) of 272 K, while ^{13}CO $J = 1 - 0$ and C^{18}O $J = 1 - 0$ were observed simultaneously at a lower sideband with a system noise temperature of 145 K. The half-power beam width was 53″ at 115 GHz and the main beam efficiency was 0.5. The pointing accuracy of the telescope was better than 5″, which was derived from continuum observations of planets (Venus, Jupiter, and Saturn). The source W51D (19.2 K) was observed once per hour as a flux calibrator. The mean rms noise level of the calibrated brightness temperature was 0.4 K for ^{12}CO $J = 1 - 0$, while it was 0.2 K for ^{13}CO $J = 1 - 0$ and C^{18}O $J = 1 - 0$. Mapping observations were centered at R.A.(J2000) = $20^h17^m45^s$, decl.(J2000) = 36°46′00″ using the on-the-fly mode with a constant integration time of 14 seconds at each point. The total mapping area is $20' \times 20'$ in ^{12}CO $J = 1 - 0$, ^{13}CO $J = 1 - 0$, and C^{18}O $J = 1 - 0$, with a $0.'5 \times 0.'5$ grid. The standard chopper wheel calibration technique is used to measure antenna temperature T_A^* corrected for atmospheric absorption (Kutner & Ulich 1981). The final data were recorded at a brightness temperature scale of T_{mb} (K). The data were reduced using the GILDAS/CLASS[5] package.

3. Results

3.1. Infrared and Radio Continuum Images

Figure 1 shows a composite three-color image of Sh2-104. The three infrared bands are the *WISE* 3.4 μm (in blue), 12 μm (in green), and 22 μm (in red). The *WISE* 12 μm band contains polycyclic aromatic hydrocarbon (PAH) emission at 11.2 μm and 12.7 μm (Tielens 2008). The PAH molecules are excited by the UV radiation from the H II region, but are easily destroyed inside the ionized region. Hence, the *WISE* 12 μm band similar to the *Spitzer* IRAC 8.0 μm band can be used to trace the photodissociation region (PDR), and

5 http://www.iram.fr/IRAMFR/GILDAS/

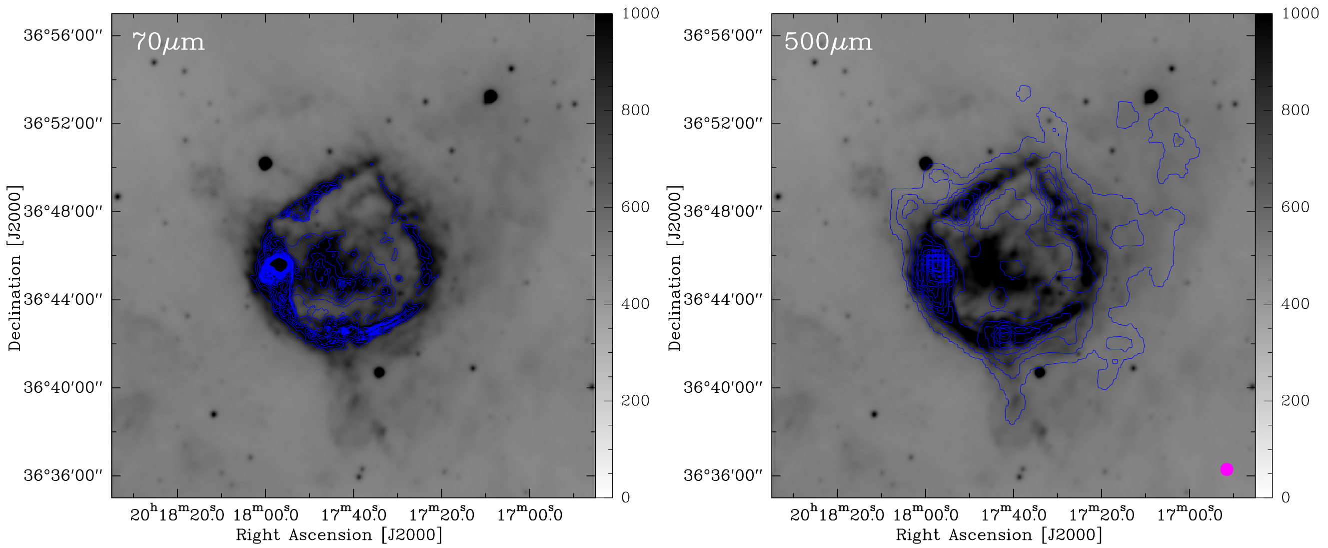

Figure 2. *Herschel* 70 μm and 500 μm emission maps superimposed on the *WISE* 12 μm emission (gray). The units for each color bar are Jy pixel^{-1}.

delineate H II region boundaries (Pomarés et al. 2009). In Figure 1, the PAH emission shows a ring-like structure with an opening toward the north. For the H II region, the *WISE* 22 μm emission traces heated small dust grains, which is similar to the MIPS 24 μm band (Anderson et al. 2014). The hot dust emission in Figure 1 displays two sources, one related to Sh2-104, and the other associated with IRAS 20160+3636.

NVSS 20 cm radio continuum emission can be used to trace ionized gas, which is also overlaid in Figure 1 by black contours. The ionized gas emission in Figure 1 indicates that Sh2-104 is a shell-like H II region, whose radius is about 2$'$.5, marked by a white dashed circle. Moreover, the ionized gas emission is spatially coincident with the hot dust emission observed at the *WISE* 22 μm (red color). Both the ionized gas and hot dust emission are enclosed by the PAH emission. Extending toward the east, a UCH II region is located at the eastern border of Sh2-104, which is related to source IRAS 20160+3636.

The 70 μm emission is mostly produced by relatively hot dust (Faimali et al. 2012), and partly corresponds to cool dust emission (Anderson et al. 2012). Figure 2 (left panel) is the 70 μm emission map, overlaid with the *WISE* 12 μm emission. The 70 μm emission also displays the ring-like shape. The ring may represent the cool dust emission, which is spatially associated with the PAH emission. Inside the ring, there is an arc-like structure. From Figures 1 and 2 (left), it is seen that the arc is spatially coincident with the 20 cm radio continuum emission, indicating that this part of the 70 μm emission is produced from the hot dust. The 500 μm emission originates from cool dust, with an average temperature of 26 K along the PDR (Anderson et al. 2012). Figure 2 (right panel) shows the 500 μm emission map superimposed on the *WISE* 12 μm emission. The 500 μm emission also shows the ring-like structure. Compared with the 12 and 70 μm emission ring, it becomes more extended from the 500 μm emission. In Figure 2 (right panel), the cool dust is mainly concentrated in four large dust clumps that are regularly distributed at the ring-like structure around Sh2-104.

3.2. CO Molecular Emission

Compared with dust continuum emission, CO emission with velocity information can be used to separate whether the projected molecular gas is associated with a H II region. To analyze the morphology of molecular gas consistent with H II region Sh2-104, here we use ^{12}CO $J = 1 - 0$, ^{13}CO $J = 1 - 0$, and C^{18}O $J = 1 - 0$ lines to trace the molecular gas. The C^{18}O $J = 1 - 0$ emission was detected in some points with strong ^{13}CO $J = 1 - 0$ emission, suggesting that these positions are more dense. Since the C^{18}O $J = 1 - 0$ signal is so weak, we do not examine its spatial distribution. Compared with the optically thick ^{12}CO line, the ^{13}CO line is more suited to tracing relatively dense gas. Using channel maps of the ^{13}CO line, we the inspect gas component for our studied region. Georgelin et al. (1973) found that the LSR velocity of the ionized gas for Sh2-104 is about 0 km s^{-1}. The ^{12}CO $J = 1 - 0$ and ^{13}CO $J = 1 - 0$ emission from -3.4 to 4.2 km s^{-1} is therefore found to be associated with Sh2-104. Figure 3 shows the integrated intensity images of ^{12}CO $J = 1 - 0$ and ^{13}CO $J = 1 - 0$, integrated over the velocity range from -3.4 to 4.2 km s^{-1}. Both the ^{12}CO $J = 1 - 0$ and ^{13}CO $J = 1 - 0$ emission exhibit a ring-like shape, but the ring traced by ^{12}CO $J = 1 - 0$ is more diffuse than that of ^{13}CO $J = 1 - 0$. In addition, in Figure 3, the ^{12}CO $J = 1 - 0$ and ^{13}CO $J = 1 - 0$ emission coincide well with the PDR traced by the PAH emission surrounding Sh2-104. It is apparent that the PDR is thinner compared to the CO isotopologue emission. Inside the ring, we did not detect stronger CO emission, which is similar to what is observed in ^{12}CO $J = 2 - 1$ (Deharveng et al. 2003). Figure 4 shows the ^{13}CO $J = 1 - 0$ spectra on top of its integrated intensity map. It is obvious that the spectra are not higher than the baseline signal inside the ring, which is different from that for H II region RCW 120. Inside RCW 120, Anderson et al. (2015) detected multiple velocity components in ^{13}CO $J = 1 - 0$.

To investigate spatial correlation between the gas and dust of the ring around Sh2-104, we overlaid the ^{13}CO $J = 1 - 0$ integrated intensity map on the *Herschel* 500 μm emission (Figure 5). The ^{13}CO $J = 1 - 0$ emission in Figure 5 is associated with the 500 μm dust emission in morphology.

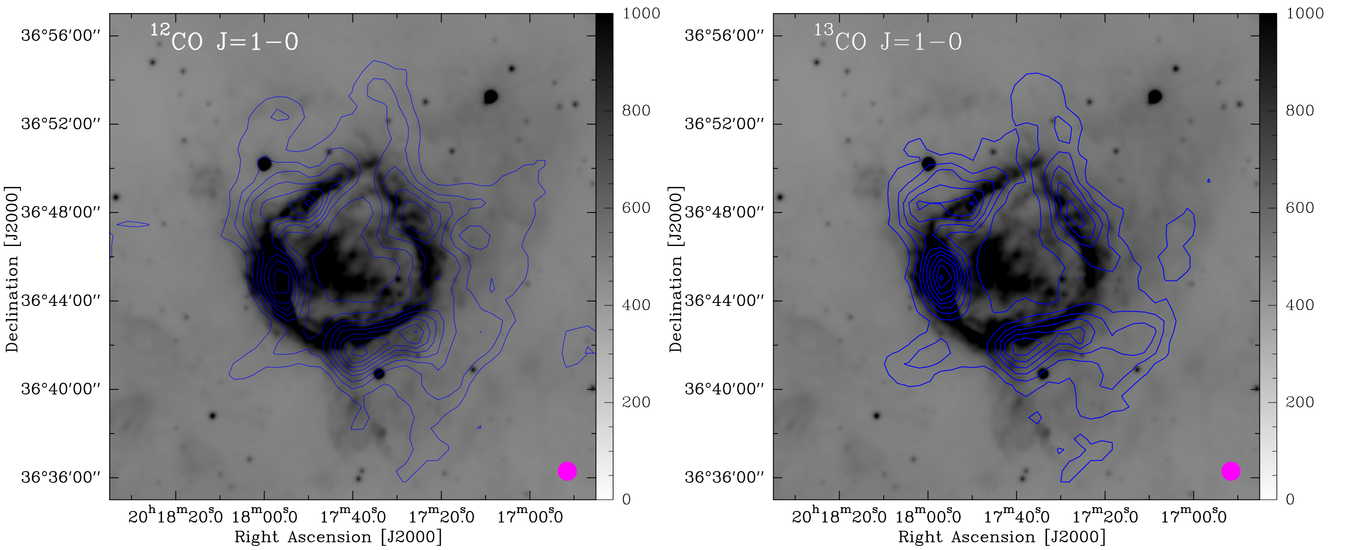

Figure 3. Left panel: contours of ^{12}CO $J = 1 - 0$ emission superimposed on the 12 μm emission map (gray). The integrated velocity is from −3.4 to 4.2 km s^{-1}. The blue contour levels are from 14.7 (3σ) to 66.2 by a step of 7.3 K km s^{-1}. Right panel: contours of ^{13}CO $J = 1 - 0$ emission superimposed on the 8 μm emission map (gray). The blue contour levels are from 1.8 (3σ) to 16.2 by a step of 1.8 K km s^{-1}.

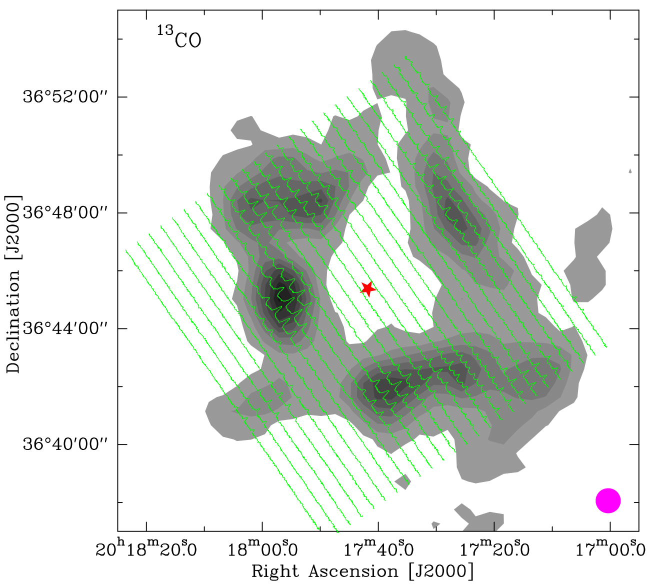

Figure 4. ^{13}CO $J = 1 - 0$ spectra overlaid in the integrated intensity image of ^{13}CO $J = 1 - 0$.

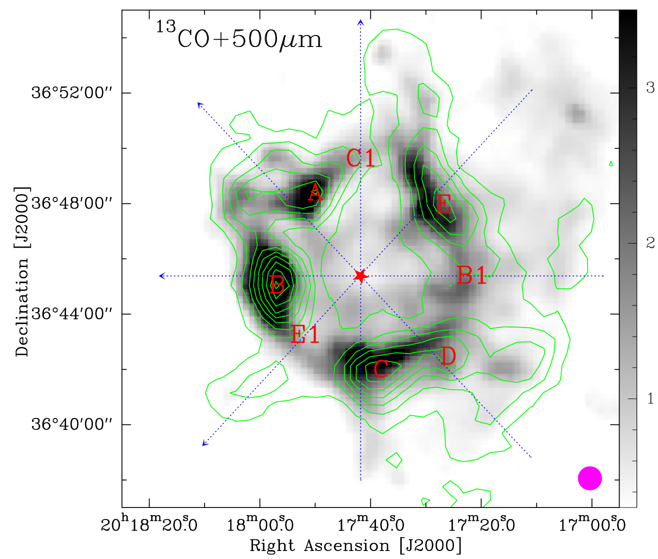

Figure 5. ^{13}CO $J = 1 - 0$ integrated intensity map overlaid on the *Herschel* 500 μm image (color scale). The green contour levels are from 1.8 (3σ) to 16.2 by a step of 1.8 K km s^{-1}. Letters A, B, C, and D indicate the different molecular clumps, while letters A1, B2, C1, and D1 represent the symmetrical position with these clumps in the ring. The red "star" represents the exciting star. The data used in the position–velocity diagrams (in Figure 6) are selected along the blue arrows. The unit for the color bar is Jy pixel^{-1}.

There are four gas fragments located in the ring. These fragments are different from dust fragments; the southern gas fragment contains two clumps. We have designated these clumps as clump A, clump B, clump C, clump D, and clump E. Clump B is more compact relative to the other clumps, which is spatially consistent with IRAS 20160+3636. Figure 6 shows the ^{12}CO $J = 1 - 0$, ^{13}CO $J = 1 - 0$, and C^{18}O $J = 1 - 0$ spectra toward the peak position of each clump. The line profiles of ^{12}CO $J = 1 - 0$ and ^{13}CO $J = 1 - 0$ in clump B appear to only show the blue wings, while the profiles display the blue and red winds in clump E. For clumps C and D, the line profiles of ^{12}CO $J = 1 - 0$ and ^{13}CO $J = 1 - 0$ show two velocity components. We fitted each spectrum with the Gaussian profile. Table 1 shows the fitted results, including their peak intensities, FWHMs, and central velocities. From Table 1, we can see that the central velocities of these clumps are different. As shown in the Figure 6, the central velocity of each clump has a shift with respect to the LSR velocity of the ionized gas for Sh2-104, except for clump A.

3.3. The Column Density and Mass of Molecular Ring

To estimate the column density and mass of the molecular ring around Sh2-104, we used the optical thin ^{13}CO $J = 1 - 0$ emission. Assuming local thermodynamical equilibrium, the column density was estimated via Garden et al. (1991) as

$$N(^{13}\mathrm{CO}) = 4.71 \times 10^{13} \frac{T_{\mathrm{ex}} + 0.88}{\exp}(-5.29/T_{\mathrm{ex}}) \times \frac{\tau}{1 - \exp(-\tau)} \mathrm{~W~cm^{-2}}, \quad (1)$$

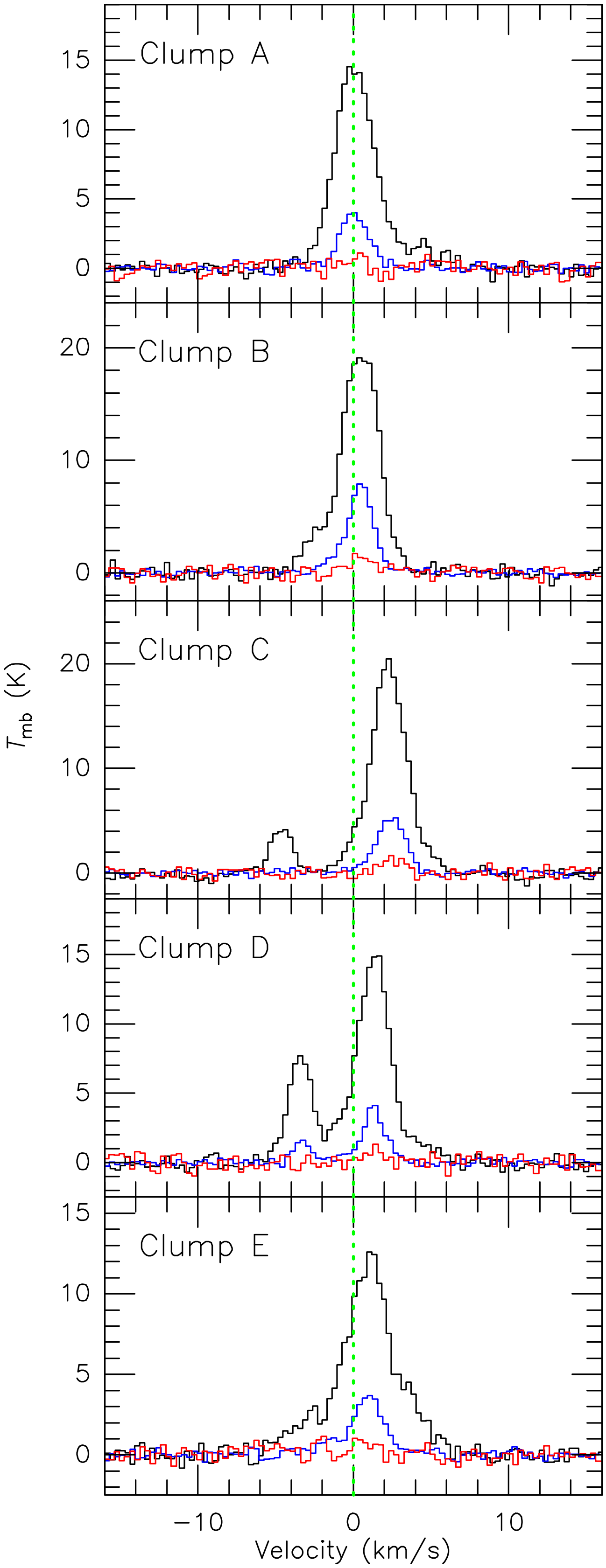

Figure 6. ^{12}CO $J = 1 - 0$, ^{13}CO $J = 1 - 0$, and C^{18}O $J = 1 - 0$ spectra at the peak positions of molecular clumps A, B, C, D, and E. The green dashed line indicates the systemic velocity (0 km s^{-1}) of Sh2-104.

Table 1
Observed Parameters of Each Line for Each Clump

Name	^{12}CO $J = 1 - 0$			^{13}CO $J = 1 - 0$		
	T_{mb} (K)	FWHM (km s^{-1})	V_{LSR} (km s^{-1})	T_{mb} (K)	FWHM (km s^{-1})	V_{LSR} (km s^{-1})
A	14.4	3.1	0.1	4.0	2.0	0.1
B	19.6	2.9	0.5	7.7	2.0	0.6
C	19.5	2.8	2.3	5.3	2.2	2.4
D	14.3	2.7	1.3	3.8	1.8	1.3
E	11.0	4.0	1.0	3.5	2.6	1.0

where τ is the optical depth and T_{ex} is the mean excitation temperature of the molecular gas. W is $\int T_{mb} dv$ in units of K km s^{-1}, T_{mb} is the corrected main beam temperature of ^{13}CO $J = 1 - 0$, and dv is the velocity range.

Generally, the ^{12}CO emission is optically thick, so we used ^{12}CO to estimate T_{ex} via following the equation (Garden et al. 1991):

$$T_{ex} = \frac{5.53}{\ln[1 + 5.53/(T_{mb} + 0.82)]}, \tag{2}$$

where T_{mb} is the corrected main beam brightness temperature of ^{12}CO. From this equation, we derived that the excitation temperature of the five clumps is from 14.4 to 23.1 K. Since these clumps are regularly located in the ring, we adopt a mean excitation temperature of about 19.2 K as that of the molecular ring.

Moreover, we assumed that the excitation temperatures of ^{12}CO and ^{13}CO have the same value in the molecular ring. The optical depth (τ) can be derived using the following equation (Garden et al. 1991):

$$\tau(^{13}\mathrm{CO}) = -\ln\left[1 - \frac{T_{mb}}{5.29/[\exp(5.29/T_{ex}) - 1] - 0.89}\right]. \tag{3}$$

The obtained optical depth is 0.25–0.67, suggesting that the ^{13}CO emission is optically thin in the ring.

In addition, we used the relation $N(H_2)/N(^{13}CO) \approx 7 \times 10^5$ (Castets et al. 1982) to estimate the H_2 column density. The mass of the ring can be determined by

$$M_{H_2} = \mu m_H N(H_2) S, \tag{4}$$

where $\mu = 2.72$ is the mean molecular weight, m_H is the mass of a H atom, and S is the projected 2D area of the ring. Hence, we found that the mean column density of the ring is 6.8×10^{21} cm^{-2}. Using the mean column density, we derived a mass of $\sim 2.2 \times 10^4\ M_\odot$ for the ring.

3.4. Clump Extraction

Clumps with star formation activity are always found on the border of an H II region. The Hi-GAL survey data can be used to construct a column density (N_{H_2}) map of the studied region. From the column density map, we can extract clumps. Previous methods obtained column density maps at the 36."3 resolution of SPIRE 500 μm. To reveal more small structures, Palmeirim

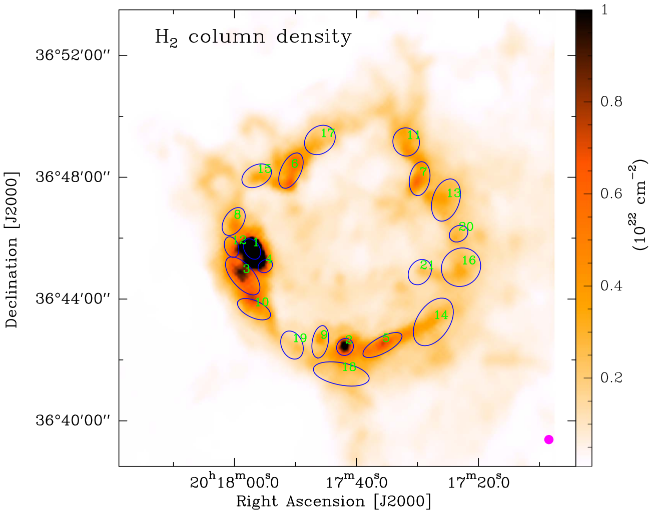

Figure 7. High-resolution (18.″2) column density map of the Sh2-104 region derived from Hi-GAL survey data. The blue ellipses indicate the identified clumps.

et al. (2013) constructed a column density map at the 18.″2 resolution of the SPIRE 250 μm data for the B211+L1495 region. Within the region covered by both PACS and SPIRE, the reliability of the smoothed 250 μm version agrees with that at the smoothed 500 μm. Based on the smoothed 250 μm method of Palmeirim et al. (2013), the column density maps of Sh2-104 were created using a modified blackbody model to fit the SEDs pixel by pixel. We only use five bands from Hi-GAL: 160, 250, 350, and 500 μm. Emission at 70 m was excluded in the SED fitting because it can be contaminated by emission from small grains in hot PDRs. The dust opacity law is assumed as $\kappa_{\upsilon} = 0.1 \times (300\ \mu\mathrm{m}/\lambda)^{\beta}\ \mathrm{cm^2\ g^{-1}}$, with $\beta = 2$. The corresponding column density map of Sh2-104 is given in Figure 7, which shows a ring-like structure. The column density of the ring ranges from $\sim 10^{21}\ \mathrm{cm^{-2}}$ to $\sim 10^{22}\ \mathrm{cm^{-2}}$. Using the ^{13}CO $J = 1 - 0$ molecular line, the obtained mean column density of the ring is $6.8 \times 10^{21}\ \mathrm{cm^{-2}}$, which is in agreement with that from Hi-GAL data.

We use the algorithm Gaussclumps (Stutzki & Guesten 1990; Kramer et al. 1998; Zhang et al. 2017) to extract clumps and derive their physical properties from the column density map. Gaussclumps is a task included in the GILDAS package. Although Gaussclumps was originally written to decompose a three-dimensional data cube into Gaussian-shaped sources, it can also be applied to dust continuum or column density maps without modification of the code. Kramer et al. (1998) suggested that the stiffness parameters that control the fitting were set to 1. A peak flux density threshold was set to 5σ. According to Belloche et al. (2011), the initial guesses for the aperture cutoff, the aperture FWHM, and the source FWHM were adopted as 8, 3, and 1.5 times the angular resolution, respectively. In Table 2, we display all the clumps identified with Gaussclumps. The columns are organized as follows: (1) identification number of the clumps; (2) and (3) J2000 positions; (4) and (5) the major and minor deconvolved FWHM of the clumps; (6) the effective deconvolved radii; (7) and (8) H_2 column density and mass; (9) H_2 volume density.

3.5. Size, Mass, and Volume Density

Using the major and minor deconvolved FWHM (θ_{maj} and θ_{min}) of the clumps, the effective deconvolved radii of these clumps was determined by

$$R_{\mathrm{eff}} = \sqrt{\theta_{\mathrm{min}} \times \theta_{\mathrm{maj}}}/2. \tag{5}$$

The obtained R_{eff} are listed in column 6 of Table 2. Clump radii are found to lie between 0.19 pc and 0.77 pc.

In addition, the total mass of the clumps was calculated from their H_2 column densities (Kauffmann et al. 2008),

$$M = \mu m_{\mathrm{H}} \int N_{\mathrm{H_2}} dA, \tag{6}$$

where $\mu = 2.72$ is the mean molecular weight, m_{H} is the mass of an H atom, and the surface element dA is related to the solid angle $d\Omega$ by $dA = D^2 d\Omega$, where D is the distance of the clumps.

Assuming a 3D geometry for the clumps, the average volume density of each clump was calculated as

$$n_{\mathrm{H_2}} = \frac{M}{4/3\pi R_{\mathrm{min}}^2 R_{\mathrm{maj}} \mu m_{\mathrm{H}}}, \tag{7}$$

where R_{min} and R_{maj} are the respective minor and major axes of the clumps. The obtained volume densities are listed in Table 2.

3.6. Velocity Dispersion and Virial Parameter(α)

From the H_2 column density map, 21 clumps are identified. Based on their coordinates and sizes, we search for ^{12}CO $J = 1 - 0$ and ^{13}CO $J = 1 - 0$ spectra that are located at or near the peak positions of the clumps. Moreover, we fitted the spectrum of each clump with the Gaussian profile. The fitted parameters are listed in Table 3, including brightness temperature (T_{mb}), FWHM, and centroid velocity (V_{LSR}). For clumps 9 and 21 we did not obtain the effective spectral value because of the weak signal ($\leqslant 3\sigma$). Since the ^{13}CO $J = 1 - 0$ emission is optically thin in the ring (see Section 3.3), we use the FWHM of ^{13}CO $J = 1 - 0$ to calculate the one-dimensional velocity dispersion (σ_{υ}). Because these clumps are distributed mainly over the molecular ring associated with Sh2-104, we also need to consider the thermal velocity dispersion. σ_{υ} in each clump is calculated as follows:

$$\sigma_{\upsilon} = \sqrt{\sigma_{\mathrm{Therm}}^2 + \sigma_{\mathrm{NT}}^2}, \tag{8}$$

where σ_{Therm} and σ_{NT} are the thermal and non-thermal one-dimensional velocity dispersions. For all the clumps, σ_{Therm} and σ_{NT} can be derived as, respectively,

$$\sigma_{\mathrm{Therm}} = \sqrt{\frac{kT_{\mathrm{ex}}}{m_{\mathrm{H}}\mu}}, \tag{9}$$

$$\sigma_{\mathrm{NT}} = \left[\sigma_{^{13}\mathrm{CO}}^2 - \frac{kT_{\mathrm{ex}}}{m_{^{13}\mathrm{CO}}\mu}\right]^{1/2}, \tag{10}$$

where T_{ex} is the excitation temperature of the clumps. We used ^{12}CO $J = 1 - 0$ to calculate T_{ex} following Equation (2). $\sigma_{^{13}\mathrm{CO}} = (\Delta V_{13}/\sqrt{8 \ln 2})$ is the one-dimensional velocity dispersion of ^{13}CO $J = 1 - 0$, while $m_{^{13}\mathrm{CO}}$ is the mass of ^{13}CO $J = 1 - 0$. The derived parameters are summarized in Table 3.

The stability of the clumps against gravitational collapse can be evaluated using the virial parameter (Kauffmann et al. 2013)

$$\alpha = 1.2\left(\frac{\sigma_{\upsilon}}{\mathrm{km\ s^{-1}}}\right)^2 \left(\frac{R_{\mathrm{eff}}}{\mathrm{pc}}\right) \left(\frac{M}{10^3 M_{\odot}}\right)^{-1}, \tag{11}$$

Table 2
Derived Parameters of Identified Clumps

ID	R.A. (J2000)	Decl. (J2000)	θ_{min} (arcsec)	θ_{maj} (arcsec)	R_{eff} (pc)	N_{H_2} (10^{22} cm^{-2})	Mass ($M_\odot$)	n_{H_2} (cm^{-3})
1	20:17:54.7	36:45:38.5	30.0	43.7	0.30	2.8	251.1	5225
2	20:17:42.5	36:42:25.5	31.8	34.9	0.27	1.1	82.6	1912.2
3	20:17:55.9	36:44:45.7	43.7	91.3	0.58	1.0	330.0	1097.1
4	20:17:53.0	36:45:04.9	24.1	30.5	0.19	0.8	29.8	2317.7
5	20:17:37.6	36:42:29.3	31.6	85.9	0.45	0.7	151.4	1270.6
6	20:17:49.6	36:48:13.2	39.1	75.0	0.49	0.7	156.8	843.6
7	20:17:32.7	36:47:57.3	39.8	67.5	0.46	0.6	127.4	737.6
8	20:17:57.1	36:46:32.8	37.9	60.6	0.42	0.5	89.9	664.2
9	20:17:45.7	36:42:35.7	31.6	64.6	0.39	0.4	67.3	766.9
10	20:17:54.4	36:43:40.1	52.2	55.9	0.49	0.5	111.2	413.4
11	20:17:34.5	36:49:09.7	27.0	42.1	0.27	0.6	42.8	1328.1
12	20:17:57.4	36:45:42.4	52.9	86.2	0.63	0.4	155.9	353.1
13	20:17:29.2	36:47:15.2	64.2	104.6	0.77	0.4	218.1	263.1
14	20:17:30.9	36:43:15.0	73.5	79.8	0.72	0.3	169.3	202
15	20:17:54.1	36:48:03.0	52.5	65.4	0.54	0.3	88.7	273.9
16	20:17:27.3	36:45:02.7	41.6	57.8	0.44	0.3	51.1	312.3
17	20:17:45.8	36:49:13.5	42.0	53.1	0.42	0.2	41.5	273.4
18	20:17:43.0	36:41:32.4	33.4	70.1	0.42	0.5	83.5	738.3
19	20:17:49.5	36:42:29.3	41.5	62.2	0.46	0.4	78.5	446.3
20	20:17:27.6	36:46: 8.9	43.7	111.7	0.64	0.3	121.3	328.5
21	20:17:32.7	36:44:53.1	30.6	38.7	0.28	0.2	19.2	439.3

where σ_v is the one-dimensional velocity dispersion, R_{eff} is the effective deconvolved radius, and M is the mass of the clumps. If $\alpha \leqslant 2$, the clumps collapse (Bertoldi & McKee 1992; Kauffmann et al. 2013). Hence, from Table 3, we obtain that clumps 1, 3, and 10 collapse.

3.7. Distribution of Young Stellar Objects (YSOs)

To detect YSOs adjacent to Sh2-104, we use the *WISE* and 2MASS all-sky source catalogs (Skrutskie et al. 2006; Wright et al. 2010). From these two catalogs, we select the sources with the 3.4, 4.6, 12, and 22 μm, and *J*, *H*, and *Ks* bands within a circle of 9′ in radius centered on the ionized star of Sh2-104. We select YSOs using the criteria described in Koenig & Leisawitz (2014), as shown in Figure 8. These criteria are based on the [4.6]–[12.0] versus [3.4]–[4.6] color–color, and $[Ks] - [3.4]$ versus [3.4]–[4.6] color–color diagrams. Since many objects that are visible in *WISE* bands 1 and 2 will lack a reliable band 3 or 4 detection, the [3.4]–[4.6] versus $[H] - [Ks]$ color–color diagram is a supplement to the [4.6]–[12.0] versus [3.4]–[4.6] color–color diagram. Based on the above color selection criteria of YSOs, we only find 3 Class I YSOs and 8 Class II YSOs. Furthermore, a much cleaner selection technique has been used by Marton et al. (2016) to create an all-sky catalog of YSOs (Class I/II). According to the catalog of Marton et al. (2016), we find 23 Class I/II YSOs. Comparing the YSO positions, there is only one YSO overlap between the two methods. Class I YSOs are protostars with circumstellar envelopes, while Class II YSOs are disk-dominated objects (Evans et al. 2009). The *J* luminosity is used to estimate stellar masses, as *J* is less affected by the emission from circumstellar material (Bertout et al. 1988; Yadav et al. 2016). Figure 9 shows the $J/J - H$ color–magnitude diagram for the selected YSOs. The black solid curve denotes the location of 10^6 yr pre-main-sequence (PMS) stars, and the blue solid curve is for those that are 1.5×10^6 yr, both of which were obtained from the model of Siess et al. (2000). All the isochrones are corrected for the distance and reddening of the Sh2-104 region. The dashed lines represent reddening vectors for various masses. The black dashed line denotes the position of a PMS star with 1.8 $M_\odot$ for 1.0 Myr, and the blue dashed lines indicate the position of a star with 6.0 $M_\odot$ for 0.15 Myr. From Figure 9, we see that the majority of the YSOs have masses in the range 1.8–6.0 $M_\odot$, and an age range of 0.15–1.0 Myr. Figure 10 shows the spatial distribution of both Class I and Class II YSOs. From Figure 10, we also note that Class I/II YSOs are mostly concentrated along the molecular and dust rings.

4. Discussion

4.1. Gas Structure around Sh2-104

The ionized gas of Sh2-104 shows a ring-like structure with a radius of about 2.9 pc (2′.5 at 4 kpc), which is consistent with the optical image (Deharveng et al. 2003). Deharveng et al. (2010) studied 102 bubbles. Only bubbles N49 and N61 show a shell-like structure in both the radio continuum emission and the 24 μm emission (Watson et al. 2008; Xu et al. 2016). They suggested that such shell-like structure could be due to a stellar wind emitted by the central massive star. Both CO molecular gas and cool dust emission show a ring-like shape, which just encloses the ionized gas of Sh2-104. If a H II region spherically expands, both the collected gas and dust emission will also show a three-dimensional spherical shell structure. However, Beaumont & Williams (2010) suggested that the collected gas and dust emission around a H II region are two-dimensional rings with thicknesses not greater than the ring sizes. For three-dimensional shells, expanding along the line of sight will result in blueshifted emission from the near side of the shell and redshifted emission from the far side (Anderson et al. 2015). Here, for the CO molecular ring surrounding H II region Sh2-104, we also did not detect CO emissionhigher than 3σ (0.6 K) inside the ring.

Table 3
Properties of Identified Clumps around the H II Region Sh2-104

ID	$T_{mb}(12)$ (K)	FWHM(12) (km s^{-1})	$V_{LSR}(12)$ (km s^{-1})	$T_{mb}(13)$ (K)	FWHM(13) (km s^{-1})	$V_{LSR}(13)$ (km s^{-1})	T_{ex} (K)	σ_{Therm} (cm^{-3})	σ_{NT}	σ_v	α
1	13.5(0.5)	3.9(0.1)	0.1(0.1)	5.4(0.2)	2.6(0.1)	−0.2(0.1)	17.0(0.5)	0.22(0.01)	1.10(0.02)	1.12(0.01)	1.8
2	12.0(1.2)	3.5(0.2)	2.5(0.1)	4.2(0.3)	2.2(0.1)	2.5(0.1)	15.4(0.5)	0.21(0.01)	0.92(0.03)	0.94(0.02)	3.5
3	16.1(0.5)	3.0(0.1)	0.6(0.1)	6.1(0.2)	1.9(0.1)	0.6(0.1)	19.6(0.5)	0.24(0.01)	0.79(0.02)	0.83(0.01)	1.5
4	17.2(0.5)	3.3(0.1)	0.4(0.1)	6.3(0.2)	2.2(0.1)	0.2(0.1)	20.7(0.5)	0.25(0.01)	0.94(0.02)	0.97(0.01)	7.2
5	15.2(1.7)	2.4(0.1)	1.7(0.1)	4.6(0.3)	1.8(0.1)	1.7(0.1)	18.7(0.5)	0.23(0.11)	0.77(0.02)	0.80(0.01)	2.3
6	15.2(1.2)	3.3(0.1)	0.6(0.1)	4.2(0.3)	2.6(0.1)	0.5(0.1)	18.7(0.5)	0.23(0.01)	1.09(0.03)	1.12(0.02)	4.7
7	5.3(0.5)	6.2(0.2)	0.3(0.1)	2.1(0.3)	2.4(0.2)	0.6(0.1)	8.6(0.5)	0.16(0.01)	1.02(0.08)	1.03(0.04)	4.6
8	9.7(0.5)	4.0(0.1)	0.1(0.1)	2.0(0.3)	3.5(0.2)	−0.1(0.1)	13.1(0.5)	0.20(0.01)	1.47(0.07)	1.48(0.04)	12.3
9	…	…	…	…	…	…	…	…	…	…	…
10	9.1(0.8)	2.8(0.2)	1.0(0.1)	3.8(0.3)	1.4(0.1)	1.1(0.1)	12.5(0.8)	0.19(0.01)	0.59(0.03)	0.62(0.01)	2.0
11	9.9(0.5)	3.1(0.1)	1.0(0.1)	2.4(0.3)	2.1(0.1)	0.8(0.1)	13.3(0.5)	0.20(0.01)	0.90(0.05)	0.92(0.02)	6.4
12	8.5(0.5)	4.4(0.1)	−0.4(0.1)	2.8(0.3)	3.2(0.1)	−0.4(0.1)	11.8(0.5)	0.19(0.01)	1.38(0.05)	1.40(0.02)	9.5
13	8.9(0.6)	5.2(0.1)	1.2(0.1)	2.3(0.3)	2.4(0.2)	1.7(0.1)	12.3(0.6)	0.19(0.01)	1.02(0.09)	1.04(0.04)	4.6
14	8.2(0.5)	6.5(0.1)	0.3(0.1)	2.3(0.6)	1.7(0.2)	1.3(0.1)	11.6(0.5)	0.18(0.01)	0.74(0.08)	0.76(0.04)	2.9
15	15.6(0.5)	3.0(0.1)	0.4(0.1)	4.3(0.3)	2.2(0.1)	0.3(0.1)	19.1(0.5)	0.24(0.01)	0.92(0.02)	0.95(0.01)	6.6
16	3.6(0.5)	9.7(0.1)	0.7(0.1)	0.9(0.3)	3.0(0.5)	3.7(0.2)	6.8(0.5)	0.14(0.01)	1.27(0.20)	1.28(0.10)	16.9
17	8.9(0.6)	3.3(0.2)	0.1(0.1)	2.6(0.3)	2.2(0.1)	−0.2(0.1)	12.3(0.6)	0.19(0.01)	0.91(0.05)	0.93(0.02)	10.5
18	16.8(1.2)	2.7(0.1)	2.4(0.1)	4.1(0.3)	2.0(0.1)	2.6(0.1)	20.3(0.5)	0.24(0.01)	0.82(0.03)	0.86(0.01)	4.5
19	6.0(0.5)	2.8(0.1)	0.7(0.1)	0.7(0.3)	3.4(0.4)	0.5(0.2)	9.3(0.5)	0.17(0.01)	1.43(0.18)	1.44(0.09)	14.6
20	4.1(0.5)	7.3(0.2)	−0.7(0.1)	1.2(0.3)	2.2(0.3)	−2.2(0.1)	7.4(0.5)	0.15(0.01)	0.92(0.13)	0.93(0.07)	5.5
21	…	…	…	…	…	…	…	…	…	…	…

To further reveal the structure of the ring, we made four position–velocity (PV) diagrams in the ^{13}CO $J = 1 - 0$ line, as shown in Figure 11. These PV diagrams are obtained from the four cuts through the position of the exciting star with the position angles (PAs) of 0°, 45°, 90°, and 135° (see Figure 5). From Figure 11, we see that the symmetrical borders of the ring are detected along all four cuts. Each border is marked by a blue dashed line. Between two symmetrical borders, we still did not detect CO emission. Since our selected cuts just go through these identified clumps, then the position of each clump can indicate a border of the ring. For the symmetrical borders, we assign them the names clumps A1, B1, C1, D1, and E1. If one border has two CO components, the other component will be named serially, e.g., clumps A2 and B2. Through inspecting clumps A2 and B2's associations with the Sh2-104 morphology, we suggest that these two clumps should belong to the foreground emission of the corresponding border, and only overlap with the other component in the line of sight. Through the PV diagrams (Figure 11), we found that both of the borders of the ring with clumps E and E1 have a systemic velocity of about 1 km s^{-1}. The cut line through clumps E and E1 divides the ring into two portions: north–east and south–west. The north–east portion containing clumps A, B, and C1 is blueshifted, while the south–west portion with clumps B1, C, and D is redshifted. Hence, we concluded that the ring is expanding with an inclination relative to the plane of sky. The existence of the inclination indicates that the ring is not spherically symmetrical. Additionally, from Figure 11, we also see that the projected distances are the same and 7$'$.5 between two symmetrical edges along the different PAs. The distance between clumps E and E1 is roughly equal to their projected distance. The distances between clumps C and C1, clumps A and D, and clumps B and B1 are greater than 7$'$.5 because the cut lines through two symmetrical clumps have an inclination angle with the projected axis. This further suggests that the ring is not spherically symmetrical. The ionized gas of Sh2-104 has a LSR velocity of about 0 km s^{-1} (Georgelin et al. 1973), while the expansion of the molecular ring begins at a LSR velocity of 1 km s^{-1}. If there is a three-dimensional spherical shell that just encloses Sh2-104, the ionized gas and the ring should have the same LSR velocity. From the above analysis, we have concluded that the collected gas emission around H II region Sh2-104 may be a two-dimensional ring-like structure.

In addition, we also make slice profiles of the *WISE* 12 μm emission (black lines) and the H_2 column density map (blue lines) through Sh2-104 in the PA = 45 degree and PA = 135 degree directions, as shown in Figure 12, which shows the 12 μm flux and H_2 column density change as a function of the position. The two symmetrical borders (red dashed lines) of the ring related to Sh2-104 display the strange 12 μm and H_2 emission, indicating that the strange PAHs molecules traced by the 12 μm emission are excited only if there should be some molecular gas adjacent to the H II region. However, the 12 μm emission is very strange inside the ring, while the H_2 column density is lower in the corresponding positions. Compared with the 70 μm emission in the left panel of Figure 2, we that found the 12 μm emission is associated with that at 70 μm inside the ring, suggesting that this part of the 12 μm emission is also produced from the hot dust. Thus, this further confirms that the collected gas emission is likely to a two-dimensional ring-like structure around H II region Sh2-104.

4.2. Star Formation Scenario

Five large clumps are regularly spaced along the ring. One of these clumps is associated with a UCH II region and IRAS 20160+3636. Deharveng et al. (2003) suggested that the CC process is at work in this region. From the high-resolution (18$''$.2) column density map constructed by the Hi-GAL survey data, we extract 21 clumps. To determine whether the identified clumps have sufficient mass to form massive stars, we must consider their sizes and mass. According to Kauffmann & Pillai (2010), if the clump mass is $M(r) \geqslant 580\,M_\odot (r/\mathrm{pc})^{1.33}$, they can thus potentially form massive stars. Figure 13 presents a mass versus radius plot of

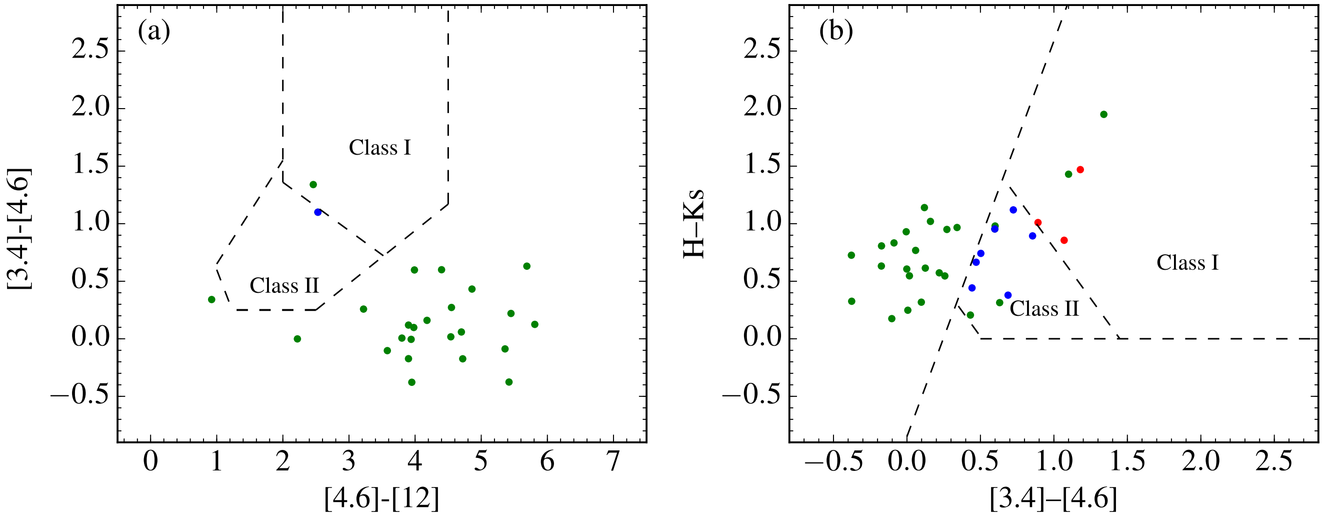

Figure 8. Left panel: *WISE* band 1, 2, 3 color–color diagram. Right panel: *WISE* bands 1 and 2 and 2MASS *H* and *Ks* color–color diagram. The dashed lines indicate the boundaries by which we classify Class I and Class II. Class I YSOs are labeled as red dots, and class II YSOs are labeled as blue dots. The green dots indicate Class I/II YSOs from (Marton et al. 2016).

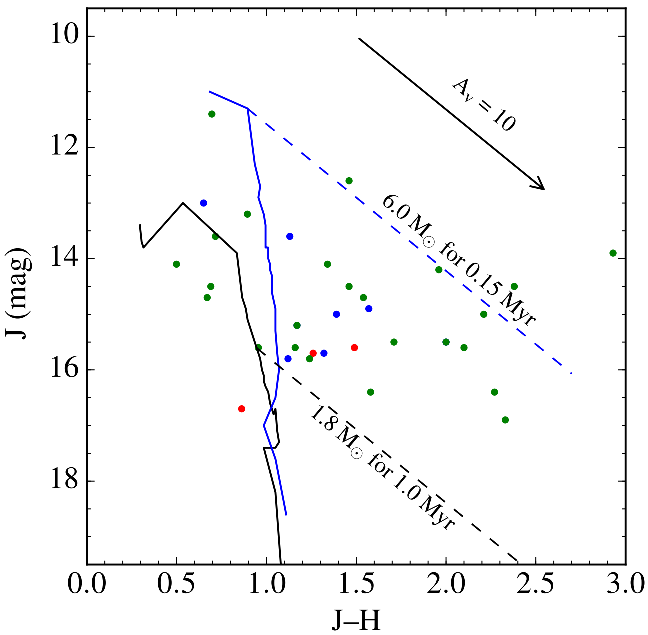

Figure 9. J/JH color–magnitude diagram for the YSOs. Class II YSOs are labeled as red dots, and Class I YSOs are labeled as blue dots. The green dots indicate Class I/II YSOs from (Marton et al. 2016). The black solid curve denotes the location of 10^6 yr PMS stars, and the blue solid curve is for those that are 1.5×10^6 yr, both of which were obtained from the model of Siess et al. (2000). All the isochrones are corrected for the distance and reddening of the Sh2-104 region. The dashed lines represent reddening vectors for various masses. The black dashed line denotes the position of a PMS star with 1.8 $M_\odot$ for 1.0 Myr, and the blue dashed lines indicate the position of a star with 6.0 $M_\odot$ for 0.15 Myr.

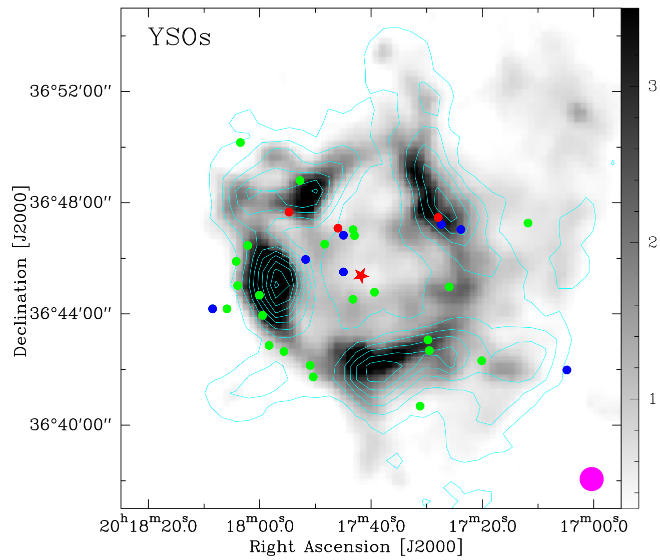

Figure 10. ^{13}CO $J = 1 - 0$ integrated intensity map overlaid on the *Herschel* 500 μm image (gray scale). Class II YSOs are labeled as red dots, and Class I YSOs are labeled as blue dots. The green dots indicate Class I/II YSOs from Marton et al. (2016). The unit for the color bar is Jy pixel^{-1}.

the clumps. We find that only two clumps (#1 and #3) are above the threshold, indicating that these two clumps are dense and massive enough to potentially form massive stars. About 90% of all the identified clumps will form low-mass stars. Moreover, we evaluate the stability of these clumps against gravitational collapse using the virial parameter, finding that only three clumps collapse, including clumps #1 and #3. The surface density of 0.024 g cm^{-2} gives the average surface density thresholds for efficient star formation. The thresholds, shown in the green lines in Figure 13, are derived by Heiderman et al. (2010) and Lada et al. (2010), respectively. As can be seen from Figure 13, 15 clumps (72%) lie at or above the lower surface density limit of 0.024 g cm^{-2}. A power-law fit to the identified clumps yields $M(r) = 281\, M_\odot (r/\mathrm{pc})^{1.31\pm0.08}$. The slope we obtained is equal to what was found in Kauffmann & Pillai (2010).

The selected YSOs (Class I and Class II) are mostly concentrated in the whole ring around H II region Sh2-104. The high density of the YSOs located in the ring show that these YSOs are physically associated with Sh2-104. The dynamical age of Sh2-104 can be used to decide whether these YSOs are triggered by the H II region. Using a simple model described by Dyson & Williams (1980) and assuming a H II region expanding in a homogeneous medium, we estimate the

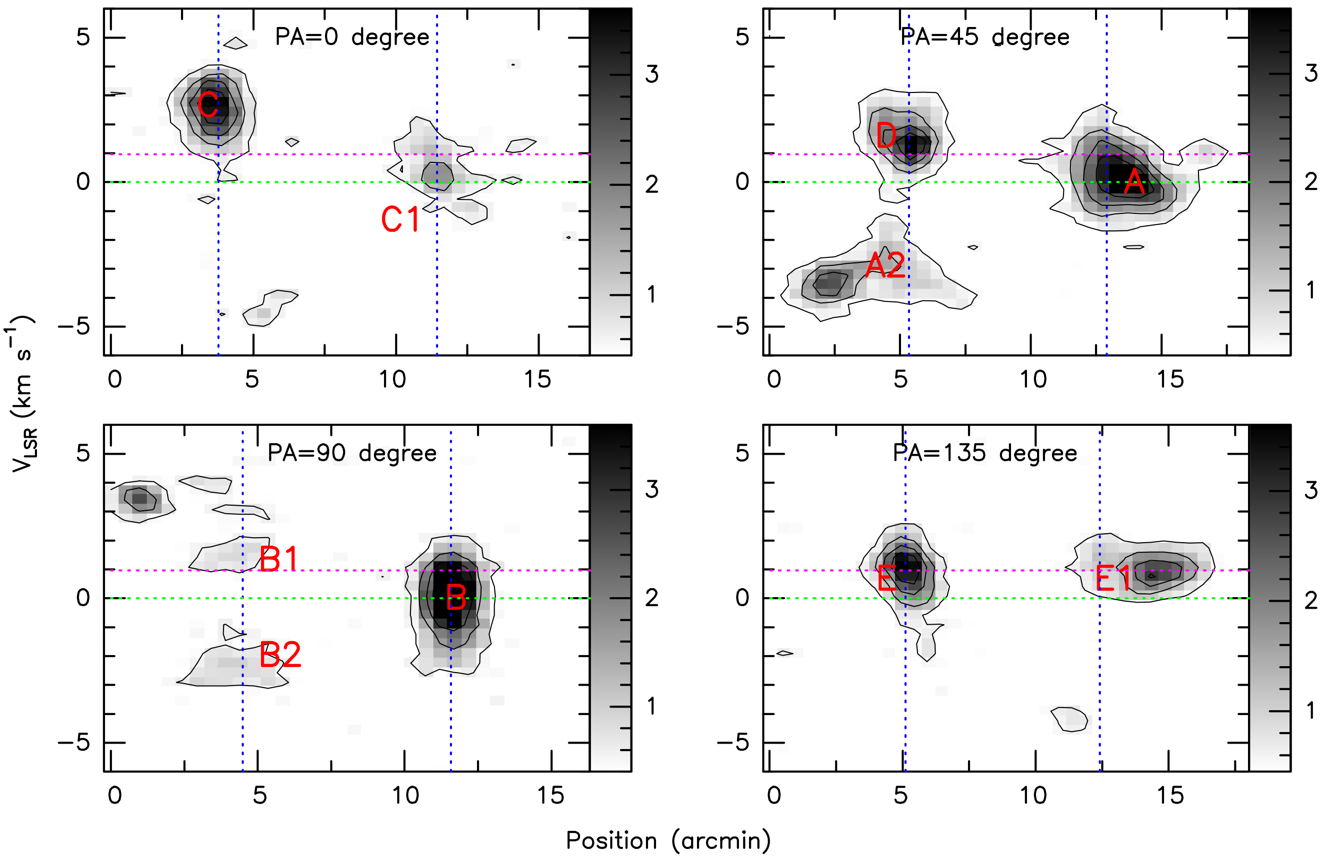

Figure 11. PV diagrams constructed from the ^{13}CO $J = 1 - 0$ transition for different directions. The contour levels are 10%, 20%,…, 90% of the peak value. The blue dashed lines show the projected position of each edge at different position angles, while the green dashed lines indicate a systemic velocity (0 km s^{-1}) of Sh2-104; The pink dashed lines indicate a systemic velocity of 1 km s^{-1}.

dynamical age of the H II region as

$$t_{\rm dyn} = \frac{4R_{\rm s}}{7c_{\rm s}}\left[\left(\frac{R}{R_{\rm s}}\right)^{7/4} - 1\right], \tag{12}$$

where $R_{\rm s}$ is the radius of the Strömgren sphere given by $R_{\rm s} = 3Q_{\rm Ly}/4\pi n_0^2\alpha_{\rm B}$, where $Q_{\rm Ly}$ is the ionizing luminosity, n_0 is the initial number density of the ambient medium around the H II region, and $\alpha_{\rm B} = 2.6 \times 10^{-13}\,{\rm cm}^3\ {\rm s}^{-1}$ is the hydrogen recombination coefficient to all levels above the ground level. For the ionized medium we adopt a sound velocity of $c_{\rm s} \simeq 10\,{\rm km\,s}^{-1}$. Moreover, we adopt the radius (3$'$.7) of the ring as that of H II region Sh2-104, which is obtained from Figure 11. Taking the distance of ∼4 kpc to Sh2-104 (Deharveng et al. 2003), the H II region radius is 4.4 pc. As a rough estimate, n_0 can be determined by distributing the total molecular mass over a sphere (e.g., Zavagno et al. 2007; Cichowolski et al. 2009; Paron et al. 2009; Anderson et al. 2015; Duronea et al. 2015). The mass of the ring is $\sim 2.2 \times 10^4\,M_\odot$. Using this mass, we only consider the number of atoms that can be ionized, so this would imply that $n_0 = 2.6 \times 10^3\,{\rm cm}^{-3}$. H II region Sh2-104 is excited by an O6V center star (Crampton et al. 1978; Lahulla 1985). For an O6V star, the ionizing luminosity ($Q_{\rm Ly}$) is $10^{48.99}\,{\rm s}^{-1}$ (Martins et al. 2005). Inoue (2001) suggested that only half of the Lyman continuum photons from the central source in a Galactic H II region ionize neutral hydrogen; the remainder are absorbed by dust grains within the ionized region. Finally, we obtain the ionizing luminosity of $10^{48.69}\,{\rm s}^{-1}$. Hence, we derived a dynamical age of 1.6×10^6 yr for the H II region Sh2-104. Additionally, from the $J/J - H$ color–magnitude diagram for the selected YSOs, we derive that the majority of the YSOs have masses in the range 1.8–6.0 $M_\odot$, and an age range of 0.15–1.0 Myr. Comparing the dynamical age of H II region Sh2-104 with that of the YSOs shown on the ring, we conclude that these YSOs are likely to be triggered by H II region Sh2-104. This also means that the CC or RDI processes induce the formation of these YSOs. Deharveng et al. (2003) suggested that H II region Sh2-104 is a typical candidate for triggering star formation by the CC process.

The expansion of Sh2-104 has collected the gas into the ring. To determine whether the fragmentation occurs around Sh2-104 via the CC process, we compute the fragmentation time of the collected gas based on the theoretical model of Whitworth et al. (1994) :

$$t_{\rm frag} = 1.56\left(\frac{\alpha_{\rm s}}{0.2}\right)^{7/11}\left(\frac{Q_{\rm Ly}}{10^{49}}\right)^{-1/11}\left(\frac{n_0}{10^3}\right)^{-5/11}\ {\rm Myr}. \tag{13}$$

The diagram of $t_{\rm frag}$ and $t_{\rm dyn}$ as a function of the initial ambient density n_0 is shown in Figure 14. In comparison, we find that the dynamical age of H II region Sh2-104 ($t_{\rm dyn} \approx 1.6$ Myr) is greater than the fragmentation time. This indicates that the ring of the collected gas has had enough time to fragment into the identified clumps during the lifetime of H II region Sh2-104.

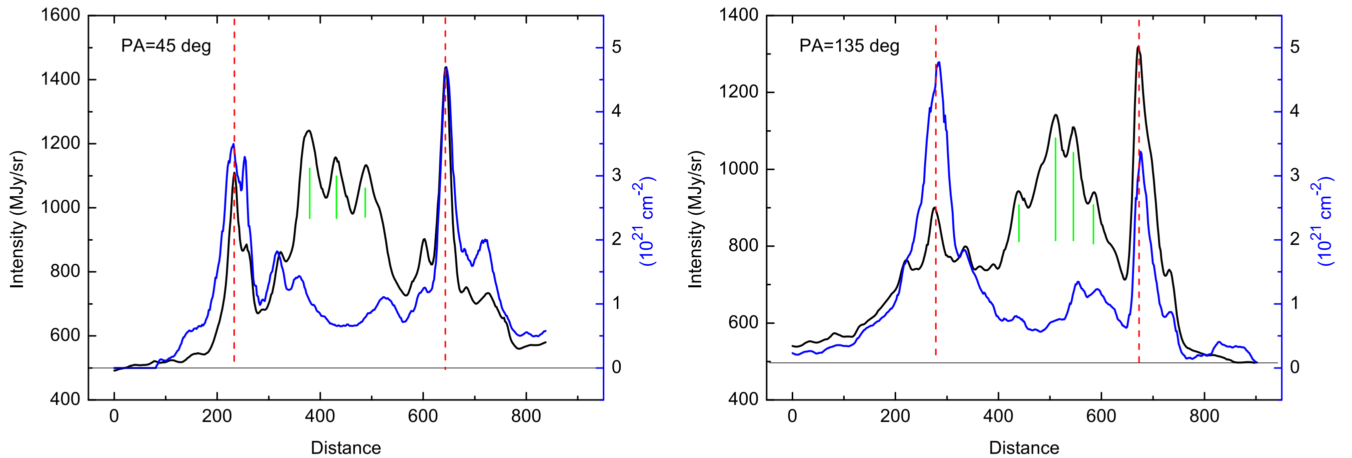

Figure 12. Slice profiles of *WISE* μm emission (black lines) and H_2 column density map (blue lines) through Sh2-104 in the PA = 45 degree and PA = 135 degree directions. The cutting paths are shown as the green arrows in Figure 11. The red dashed lines mark the two edges of Sh2-104, while the green lines may indicate some gas emission.

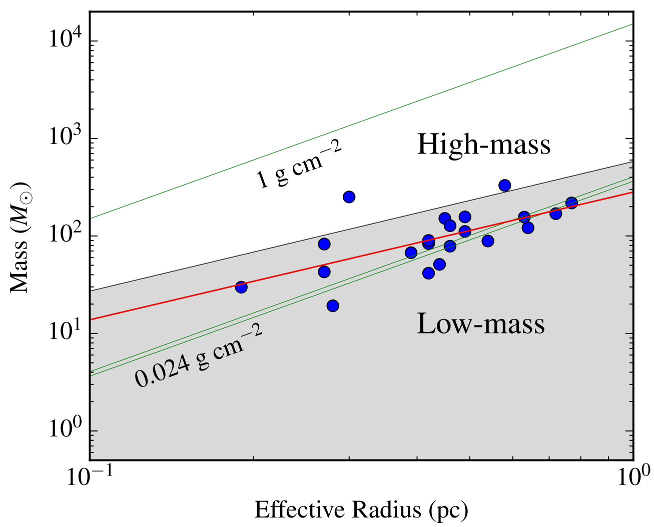

Figure 13. Mass vs. radius relationship. The gray region represents the parameter space to be devoid of massive star formation. The black line delineates the threshold (Kauffmann & Pillai 2010). The blue solid circles indicate the clumps. The upper and lower solid green lines present surface densities of 1 g cm^{-2} and 0.024 g cm^{-2}, respectively. The red line shows the result of a power-law fit to all the clumps, where we find $M(r) = 281\,M_\odot(r/\mathrm{pc})^{1.31\pm0.08}$.

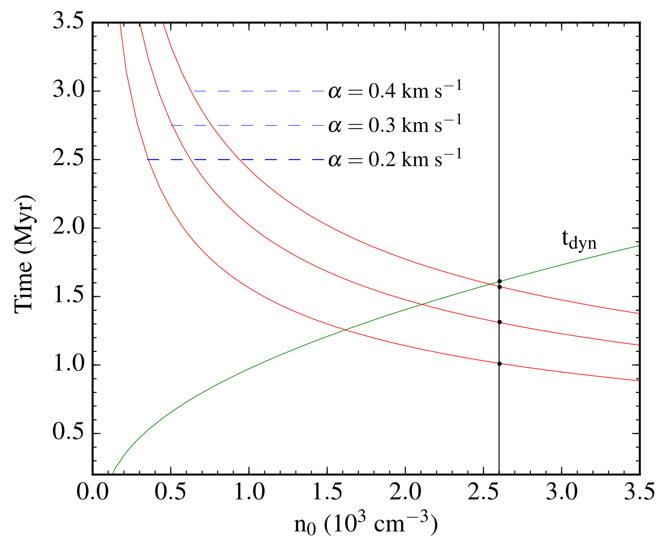

Figure 14. Plot of dynamical time (green curve) and fragmentation timescale (red curves) as a function of the initial density of the ambient medium. The fragmentation timescale is calculated for different sound speeds of neutral gas ($\alpha_s = 0.2$, 0.3, and 0.4 km s^{-1}). The black vertical line marks the position of $n_0 = 2.6 \times 10^3$ cm^{-3}.

Thus, this further confirms that the CC process is presumably at work in H II region Sh2-104.

5. Conclusions

We present the molecular ^{12}CO $J = 1 - 0$, ^{13}CO $J = 1 - 0$, and C^{18}O $J = 1 - 0$, infrared and radio continuum observations toward H II region Sh2-104. The main results are summarized as follows.

1. H II region Sh2-104 shows a double-ring structure, the outer ring traced by 12 μm, 500 μm, ^{12}CO $J = 1 - 0$, and ^{13}CO $J = 1 - 0$ emission, and the inner ring traced by 22 μm and 21 cm emission. We suggest that the outer ring with a radius of 4.4 pc is created by the expansion of H II region Sh2-104, while the inner ring with a radius of 2.9 pc may be produced by the energetic stellar wind from its central ionized star. We derived a dynamical age of 1.6×10^6 yr for H II region Sh2-104.
2. Five large clumps are found to be regularly distributed along the molecular ring. One of these clumps is associated with a UCH II region and IRAS 20160+3636. The column density and mass of the molecular ring are 6.8×10^{21} cm^{-2} and $\sim 2.2 \times 10^4\,M_\odot$. For the CO molecular ring surrounding H II region Sh2-104, we also did not detect CO emission of higher than 3σ inside the ring. The north–east portion of the ring is blueshifted relative to the LSR velocity of 1 km s^{-1}, while the south–west portion is redshifted. Hence, the ring is expanding. We concluded that the collected gas emission around H II region Sh2-104 may be a two-dimensional ring-like structure.
3. From the high-resolution (18."2) column density map constructed by the Hi-GAL survey data, we extract 21 clumps. The mass–radius relationship for the clumps shows that about 90% of all the identified clumps will form low-mass stars. Moreover, we evaluate the stability of these clumps against gravitational collapse using the

virial parameter, finding that only three clumps collapse. A power-law fit to the identified clumps yields $M = 281 M_{\odot} (r/\mathrm{pc})^{1.31 \pm 0.08}$. The slope is similar to what was found in Kauffmann & Pillai (2010).
4. The selected YSOs are distributed along the ring around H II region Sh2-104. Comparing the dynamical age of H II region Sh2-104 with the YSO timescale and the fragmentation time of the molecular ring, we further conclude that these YSOs may be triggered by H II region Sh2-104, and the CC process is at work in this region.

We thank the referee for the report, which helped to improve the quality of the paper. We are also grateful to the staff at the Qinghai Station of PMO for their assistance during the observations. This work was supported by the National Natural Science Foundation of China (Grant No. 11363004, 11403042, 11673066, and 11703040).

ORCID iDs

Chuan-peng Zhang https://orcid.org/0000-0002-4428-3183

References

Anderson, L. D., Bania, T. M., Dana, D. S., et al. 2014, ApJS, 212, 1
Anderson, L. D., Deharveng, L., Zavagno, A., et al. 2015, ApJ, 800, 101
Anderson, L. D., Zavagno, A., Deharveng, L., et al. 2012, A&A, 542, A10
Beaumont, C. N., & Williams, J. P. 2010, ApJ, 709, 791
Belloche, A., Schuller, F., Parise, B., et al. 2011, A&A, 527, A145
Bertoldi, F., & McKee, C. F. 1992, ApJ, 395, 140
Bertout, C., Basri, G., & Bouvier, J. 1988, ApJ, 330, 350
Brand, J., Massi, F., Zavagno, A., Deharveng, L., & Lefloch, B. 2011, A&A, 527, 62
Castets, A., Langer, W. D., & Wilson, R. W. 1982, ApJ, 262, 590
Cichowolski, S., Romero, G. A., Ortega, M. E., Cappa, C. E., & Vasquez, J. 2009, MNRAS, 394, 900
Condon, J. J., Cotton, W. D., Greisen, E. W., et al. 1998, AJ, 115, 1693
Crampton, D., Georgelin, Y. M., & Georgelin, Y. P. 1978, A&A, 66, 1
Deharveng, L., Lefloch, B., Kurtz, S., et al. 2008, A&A, 482, 585
Deharveng, L., Lefloch, B., Zavagno, A., et al. 2003, A&A, 408, 25
Deharveng, L., Schuller, F., Anderson, L. D., et al. 2010, A&A, 523, A6
Deharveng, L., Zavagno, A., & Caplan, J. 2005, A&A, 433, 565
Deharveng, L., Zavagno, A., & Samal, M. R. 2015, A&A, 582, A1
Duronea, N. U., Vasquez, J., Gómez, L., et al. 2015, A&A, 682, A2
Dyson, J. E., & Williams, D. A. 1980, in Physics of the Interstellar Medium, ed. J. E. Dyson & D. A. Williams (New York: Halsted Press), 204
Elmegreen, B. G., & Lada, C. J. 1977, ApJ, 214, 725
Evans, N. J., II, Dunham, M. M., Jørgensen, J. K., et al. 2009, ApJS, 181, 321
Faimali, A., Thompson, M. A., Hindson, L., et al. 2012, MNRAS, 426, 402
Garden, R. P., Hayashi, M., Hasegawa, T., et al. 1991, ApJ, 374, 540
Georgelin, Y. M., Georgelin, Y. P., & Roux, S. 1973, A&A, 25, 337
Griffin, M. J., Abergel, A., Abreu, A., et al. 2010, A&A, 518, L13
Heiderman, A., Evans, N. J., II, Allen, L. E., Huard, T., & Heyer, M. 2010, ApJ, 723, 1019
Inoue, A. K. 2001, AJ, 122, 1788
Kauffmann, J., Bertoldi, F., Bourke, T. L., Evans, N. J., II, & Lee, C. W. 2008, A&A, 487, 993
Kauffmann, J., & Pillai, T. 2010, ApJL, 723, L7
Kauffmann, J., Pillai, T., & Zhang, Q. 2013, ApJL, 765, L35
Kendrew, S., Beuther, H., Simpson, R., et al. 2016, ApJ, 825, 142
Kendrew, S., Simpson, R., Bressert, E., et al. 2012, ApJ, 755, 71
Koenig, X. P., & Leisawitz, D. T. 2014, ApJ, 791, 131
Kramer, C., Stutzki, J., Rohrig, R., & Corneliussen, U. 1998, A&A, 329, 249
Kutner, M. L., & Ulich, B. L. 1981, ApJ, 250, 341
Lada, C. J., Lombardi, M., & Alves, J. F. 2010, ApJ, 724, 687
Lahulla, J. F. 1985, A&AS, 61, 537
Martins, P. G., Schaerer, D., & Hillier, D. J. 2005, A&A, 436, 1049
Marton, G., Tóth, L. V., Paladini, R., et al. 2016, MNRAS, 458, 3479
Minh, Y. C., Kim, K.-T., Yan, C.-H., et al. 2014, JKAS, 47, 179
Molinari, S., Swinyard, B., Bally, J., et al. 2010, PASP, 122, 314
Palmeirim, P., André, Ph., Kirk, J., et al. 2013, A&A, 550, 38
Paron, S., Cichowolski, S., & Ortega, M. E. 2009, A&A, 506, 789
Poglitsch, A., Waelkens, C., Geis, N., et al. 2010, A&A, 518, L2
Pomarés, M., Zavagno, A., Deharveng, L., et al. 2009, A&A, 496, 177
Rodón, J. A., Zavagno, A., Baluteau, J.-P., et al. 2010, A&A, 518, L80
Samal, M. R., Zavagno, A., Deharveng, L., et al. 2014, A&A, 566, 122
Siess, L., Dufour, E., & Forestini, M. 2000, A&A, 358, 593
Skrutskie, M. F., Cutri, R. M., Stiening, R., et al. 2006, AJ, 131, 1163
Stutzki, J., & Guesten, R. 1990, ApJ, 356, 513
Thompson, M. A., Urquhart, J. S., Moore, T. J. T., & Morgan, L. K. 2012, MNRAS, 421, 408
Tielens, A. G. G. M. 2008, ARA&A, 46, 289
Watson, C., Povich, M. S., Churchwell, E. B., et al. 2008, ApJ, 681, 1341
Whitworth, A. P., Bhattal, A. S., Chapman, M. J., et al. 1994, MNRAS, 268, 291
Wright, E. L., Eisenhardt, P. R. M., Mainzer, A. K., et al. 2010, AJ, 140, 1868
Xu, J.-L., & Ju, B.-G. 2014, A&A, 569, 36
Xu, J.-L., Li, D., Zhang, C.-P., et al. 2016, ApJ, 819, 117
Yadav, R. K., Pandey, A. K., Sharma, S., et al. 2016, MNRAS, 461, 2502
Yuan, J.-H., Wu, Y., Li, J. Z., & Liu, H. 2014, ApJ, 797, 40
Zavagno, A., Deharveng, L., Comerón, F., et al. 2006, A&A, 446, 171
Zavagno, A., Pomarès, M., Deharveng, L., et al. 2007, A&A, 472, 835
Zhang, C.-P., Yuan, J.-H., Xu, J.-L., et al. 2017, RAA, 17, 57